

A Characteristic Dynamic Mode Decomposition

Jörn Sesterhenn¹ and Amir Shahirpour²

¹ Technical University of Berlin

² Brandenburg University of Technology (BTU)

Abstract

Temporal or spatial structures are readily extracted from complex data by modal decompositions like Proper Orthogonal Decomposition (POD) or Dynamic Mode Decomposition (DMD). Subspaces of such decompositions serve as reduced order models and define either spatial structures in time or temporal structures in space. On the contrary, convecting phenomena pose a major problem to those decompositions. A structure traveling with a certain group velocity will be perceived as a plethora of modes in time or space respectively. This manifests itself for example in poorly decaying singular values when using a POD. The poor decay is counter-intuitive, since a single structure is expected to be represented by a few modes. The intuition proves to be correct and we show that in a properly chosen reference frame along the characteristics defined by the group velocity, a POD or DMD reduces moving structures to a few modes, as expected. Beyond serving as a reduced model, the resulting entity can be used to define a constant or minimally changing structure in turbulent flows. This can be interpreted as an empirical counterpart to exact coherent structures. We present the method and its application to a head vortex of a compressible starting jet.

Keywords: Turbulent coherent structures, Modal analysis, Dynamic Mode Decomposition

1 Introduction

The proposed method in this study aims at approximating large-scale coherent structures as dynamic modes in space and time. Three topics come together: the so called coherent structures, modal decompositions, and model reduction. The constituent three parts shall be discussed briefly.

Study of coherent structures in turbulent flows has received increasing attention from scientists during the recent decades. It has become a com-

mon practice to try to understand the complex and multi-scaled nature of turbulent flows by observing the instantaneous flow fields and inspecting organized motions which possess spatial and temporal coherence. The latter implies that such motions appear at some point in time while evolving in space and remain recognizable in space in a certain time span.

Relying basically on hot wire measurements and simple flow visualization measurements, it was extremely difficult to come up with an idea of what structures are behind the observed quantities in turbulent flows. It was not until the advent of Particle Image Velocimetry (PIV) and Numerical Simulations, that the idea of a coherent structure replaced the vague eddy in literature.

Some of the first observations of coherent structures were carried out by Theodorsen in 1952 which gave rise to the notion of horseshoe eddies or hairpin vortices. His findings were later supported by many studies including the experiments of Adrian et al [2] and the simulations of Wu and Moin [31]. Such structures are observed to be originated from the wall and form Large Scale Motions (LSM) when moving in groups at the same convective velocity [1]. Similar studies have reported existence of even larger structures which scale on outer variables. They are commonly denoted in internal flows as Very Large Scale Motions and as Super Structures in external flows [5, 13]. In spite of the large range of studies carried out, many of the fundamental questions are still unanswered regarding the origin, nature and evolution of such structures.

Besides differing views on the nature and origin of turbulent structures, the suitable approach to the analysis of such structures is also still under debate. The footprints of such motions can be followed by observing the premultiplied velocity spectra which represent the energy distribution in the wave number space [21, 29]. The two peaks observed at relatively high Reynolds numbers in the outer region of the flow in the premultiplied velocity spectrum, are known to be associated with VLSM and LSM [21]. Following the spectral peaks, which can be regarded as the signature of such structures, helps to determine their length scales and energy content at different wall-normal positions, but can not provide any visualized insight into the evolution and interactions of the structures.

The availability of the strain rate tensor $S_{ij} = \frac{1}{2} \left(\frac{\partial u_i}{\partial x_j} + \frac{\partial u_j}{\partial x_i} \right)$ from numerical simulations has made the analysis and perception of such structures accessible [6] and has enabled their visualization using for instance Q criterion proposed by Hunt et al [12] and λ_2 criterion by Jeong and Hussain

[14]. They are categorized as Galilean-invariant but they fail to be invariant under more general changes such as rotation or accelerating reference frames [9].

Via a different method, Waleffe [30] looks at the coherent structures as fixed point solutions traveling in the flow. This route has been successfully followed such that today exact coherent structures can be computed for relatively high Reynolds numbers [7, 3].

On the other hand, data driven methods were adapted from other fields of science to extract structures from turbulent flows. Proper Orthogonal Decomposition (POD) was for the first time introduced to fluid dynamics by Lumley [15, 16]. POD serves as one of the methods to decompose a flow field into spatial or temporal modes which are also regarded as characteristic features of the system. Being applied to flow fields, these modes will then represent large scale energy containing structures of the flow. Bakewell and Lumley [4] were the first to apply the classical POD to experiments conducted in a turbulent pipe flow to find the dominant large scale structure of the flow in the wall region. Glauser et al [8] also applied the method to turbulent jet mixing layer and could show the existence of a large scale structure in the mixing layer containing 40% of the turbulent energy while providing proof that almost all the energy was contained in only the first three modes.

The Snapshot POD was later suggested by Sirovich [28] which was based on discretization of POD in the temporal domain and was preferable for handling time resolved CFD data. During the recent years in studies by Hellström et al [11] and Hellström and Smits [10], Snapshot POD has been applied to cross-sectional PIV measurements to visualize the structure of LSM and VLSM in turbulent pipe flow.

Although POD has proven to be a powerful tool to study turbulent coherent structures and to extract the energetic modes, but the resulted patterns lack dynamics and have problems with convective flows. The first drawback hampers the construction of reduced models of the flow, and in consequence the success of the method is limited. This problem was addressed by the introduction of Dynamical Modes by Schmid and Sesterhenn [26] and was later followed by studies by Rowley et al [24] and Schmid [25] leading to vast applications of DMD afterwards. The study by Mezić [17] provides a detailed review on DMD and its correspondence to similar approaches.

To overcome the difficulties of describing convective phenomena, several studies have focused on removing the discrete translational symmetries. One

of the first solutions was introduced by Rowley and Marsden [22] via applying a POD in a shifted frame of reference, with the traveling speed determined as a function of time $c(t)$ using template fitting and a reconstruction equation. Later in a more general framework, the study by Rowley et al [23], looked into self similar solutions by implementing both translation and scaling in space and time. More recently, Shifted POD was proposed by Reiss et al [20] aiming at model reduction by applying a shift in space to treat flows with multiple convective velocities. Regardless of the employed method to detect the group velocities, all similar works apply a spatial transformation on the dataset determined by the shift velocity.

In the present study we follow a new approach inspired by gas dynamics and the theory of characteristics. We propose to perform a modal decomposition in space and time along the characteristics. This requires a spatiotemporal transformation rather than a spatial one, and the name “Characteristic DMD” is chosen to highlight this difference. In the revision of this work, an archival version of this script was cited by Sharma et al [27], where the modes resulted from a spatiotemporal transformation are interpreted as invariant solutions of the Navier-Stokes equations.

The principal aim of this exercise is to extract low-dimensional subspaces of highly complex turbulent flows along the characteristics having the slope of the group velocities of the structures. The subspaces serve as tangential linear approximations of the nonlinear events and will accommodate the large-scale scale coherent structures in the flow. Several modes, traveling and interacting along the characteristics, shall be defined as an empirical coherent structure.

To come up with a mathematical description term, we may start off from a simple 1D problem as for example $\partial_t q + A \partial_x q = 0$ and chose a group velocity which is of particular interest to us. (In the present case it could be an eigenvalue of A , if the system is hyperbolic, but in general it is a group velocity u_g , defined differently). Next we introduce a rotated coordinate system, which points along the τ direction.

$$\xi = cx + st, \tag{1}$$

$$\tau = -sx + ct, \tag{2}$$

where $c = \cos(\theta)$ and $s = \sin(\theta)$. The angle θ corresponds to the group velocity and is defined as $\theta = u_g dt/dx$, with dt and dx being respectively the timestep between the snapshots and the spatial distance between the

points along x . Introducing the new variables, we look for the principal eigenfunctions of the system

$$\partial_\tau q + (Ic + As)^{-1}(-Is + Ac)\partial_\xi q = 0. \quad (3)$$

Several eigenfunctions with a small decay rate along τ and probably interacting (since the system is not symmetric) shall be investigated as candidates for empirical coherent structures in future work.

In what follows the method is first applied to the solutions of KDVB equation to address the problem for a one dimensional structure. In chapter 4, in order to validate the method, it has been applied to a two dimensional Lamb-Oseen vortex propagating in space and time with a known frequency and decay rate. In chapter 5, the Characteristic DMD has been implemented to detect the vortex head of a starting jet. Finally in chapter 6, a comparative analysis is carried out, to highlight the differences between a decomposition in the spatiotemporal and in a shifted frame of reference. Application of the presented method to fully turbulent structures in wall bounded flows will be the subject of a future study.

2 The Problem

From an empirical point of view a structure can be defined as an entity in space which appears somehow recognizable elsewhere at a later time. A clear example for this definition would be a solution $u(x, t) = u(x - \lambda t)$ to the convection equation

$$\partial_t u + \lambda \partial_x u = 0. \quad (4)$$

Even when non-linearly distorted, damped and dispersed, e.g. for the Korteweg – de Vries – Burgers (KDVB) equation

$$\partial_t u + u \partial_x u - \nu \partial_x^2 u + \delta \partial_x^3 u = 0, \quad (5)$$

it is possible to find an analytic solution fitting the above definition in form of a soliton. A solution of KDVB equation developing from a given initial condition will serve as an introductory example below. Even in more complex situations, for example a boundary layer, the flow exhibits structures which lack an analytic solution but clearly fit the above definition. They might be found as fixed point solutions of the Navier-Stokes equations. In what follows, we concentrate on the general case where we do not have descriptive equations yet.

The main example presented in this study will be the vortex ring of a starting supersonic jet. A long and a short high-pressure pulse being released from an orifice will be studied separately. A short pulse forms a laminar vortex ring and a long one will lead to a vortex ring followed by a jet. Both the vortex head and the jet will become turbulent provided that the Reynolds number is sufficiently high. POD, DMD or other model reduction techniques, might then be expected to easily reduce the flow and to result in a principal mode representing the structure, followed by the higher modes modifying the main mode to some degree. Unfortunately, this is not the case.

The failure can be demonstrated already for a solution of the KdVB equation (5). The chosen parameters are $\nu = 5 \times 10^{-4}$, $\delta = 4 \times 10^{-5}$ with initial condition of $u(x, 0) = 1 + \alpha e^{-(x-x_0)/\beta^2}$ where $\alpha = 0.1$ and $\beta = 0.03$. The solution at $t = 0.1$ is given in figure 1, which is distorted, damped and dispersed, but has primarily experienced a shift in x direction and would still qualify as an evolving structure in space and time. A POD of the data

$$X = [u(x, t_0), u(x, t_1), \dots, u(x, t_{n-1})] \quad (6)$$

using an SVD

$$X = U\Sigma V^T \quad (7)$$

yields the poorly reducing singular values, depicted in figure 2a. The POD-modes, being an average over all shifted solutions and necessary distortions, therefor sum up to the desired solution. This is illustrated in figure 2b. The dominant mode appears to be the swallowed elephant. Any real instance in time is made up by subtracting a large number of modes like the ones depicted in figures 2c and 2d. The resulting linear combination will not yield zero in many spatial locations and give rise to substantial spurious structure, where there should be none. A DMD along t suffers from the same problem.

3 A Remedy

The main problem above, comes neither from the nonlinearity nor the other factors, rather, the mere translation. The fact that the flow has a relatively simple structure is easily inferred from the characteristic diagram in figure 3. It can be observed that the solutions travel relatively unmolested in the direction of $\tau = x - \lambda t$.

To treat the mentioned problem for a structure traveling in time along the direction given by the wave-vector κ , the modal decomposition is to be

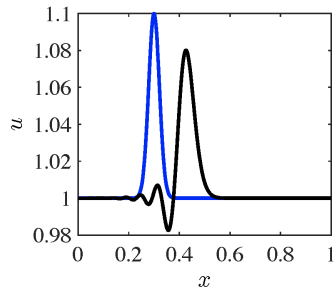


Figure 1: Solution (black) to equation 5 at $t = 0.1$ for a Gaussian initial condition (blue).

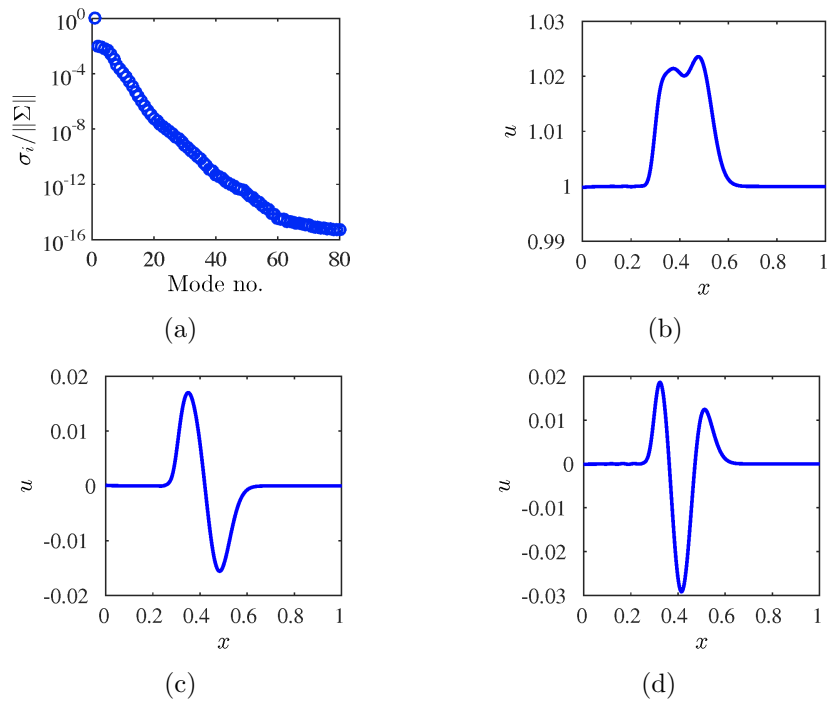


Figure 2: Singular values of snapshots of solutions to equation (6) normalized by the norm of singular values vector $\|\Sigma\|$ (a) and the first three POD modes of the solutions of the same equation (b,c,d).

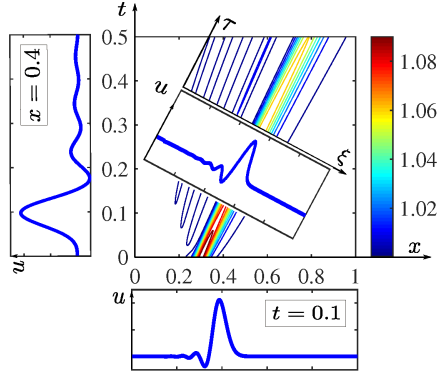


Figure 3: Spatial, temporal and spatiotemporal representation of the KdVB solutions.

sought in a plane normal to that direction in space-time

$$x_i = \{t, x_1, x_2, x_3\} \quad i = 0 \dots 3. \quad (8)$$

Given the example above, the ratio of the second to the first singular value of eq.(6) are plotted in figure 4a for decomposition in different directions. There is a dramatic drop when the proper direction is chosen for the snapshots, as also shown for the first 10 modes in figure 4b. The new frame of reference is in fact reached by transformation of snapshots matrix via a rotation in space and time, to align the new time coordinate (τ) with the direction which leads to the maximum drop of singular values. The resulted snapshots matrix will thereby accommodate the structures in spatiotemporal space as:

$$X_{0..n} = \{u(\xi, \tau_0), u(\xi, \tau_1) \dots u(\xi, \tau_n)\}. \quad (9)$$

The essence of the method presented here is to perform a modal decomposition along the direction which leads to the maximum drop of singular values and later transform the snapshots back into physical space.

After that operation, the first singular vector, shown in figure 5, looks as expected for the structure of the solution of the KdVB-equation (5). Higher modes drop off fast and minimally change the overall shape of the mode. It should be noted that figure 5a represents the spatiotemporal structure. A back transformation to physical space will be necessary to either see the temporal evolution in a given space interval as depicted in figure 5b, or conversely, the spatial changes in a time interval.

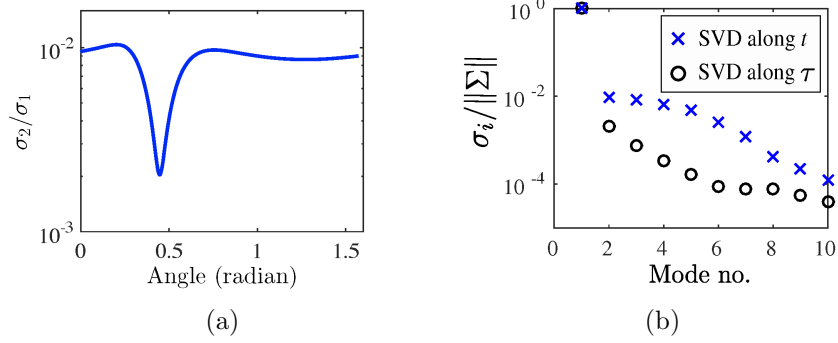


Figure 4: Ratio of singular values for SVD along different directions (a) and the first 10 normalized singular values along t and τ (b).

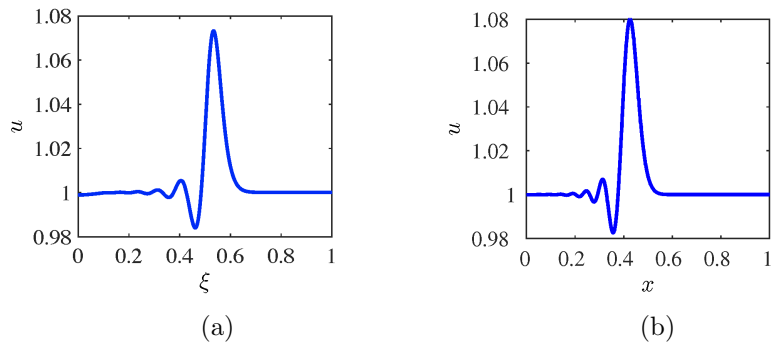


Figure 5: KdVB-Structure in spatiotemporal space (a) and physical space (b) at $t = 0.1$.

4 Validation of the Method

4.1 Detection of a traveling Lamb-Oseen vortex

In order to validate the method and to demonstrate how the decay rate and frequency of a structure can be correctly captured along the characteristics, analytical solution of Lamb-Oseen vortex is used. The tangential velocity distribution along the radius is defined as:

$$U(r) = U_{max} \left(1 + \frac{2}{2\alpha}\right) \left(\frac{R}{r}\right) \left(1 - \exp\left(\frac{-\gamma r^2}{R^2}\right)\right), \quad (10)$$

with the constant of $\gamma = 1.256$, where $U_{max,i}$ and R corresponding respectively to the initial maximum velocity and the vortex radius. While the vortex propagates in space, its maximum velocity is dictated to oscillate and decay in time as:

$$U_{max}(t) = U_{max,i} \exp(2\pi t(-d^* + f^*i)), \quad (11)$$

$$d_v^* = \frac{2dR}{U_{max,i}} = 0.01, \quad f_v^* = \frac{2fR}{U_{max,i}} = 0.08. \quad (12)$$

with d^* and f^* being the dimensionless decay rate and frequency of the vortex respectively.

The main aim of this chapter will be to detect the vortex with only one mode with the eigenvalues presenting a frequency and a decay rate similar to those of the vortex. Therefore two decompositions will be carried out for the introduced set up, one along the characteristics direction defined by the group velocity of the vortex, and the other along the time axis in physical space, in order to emphasize the differences between both sets of results.

Starting from the initial condition shown in figure 6a as contours of dimensionless velocity ($u^* = u/U_{max,i}$), the vortex propagates in space and time with the group velocity of $u_g^* = 0.2$, which is observable in the space time diagram in figure 6b. A rotation in space and time will provide the proper frame of reference aligning the new coordinates with the direction yielding the best drop of singular values. As expected, it can be clearly seen in figure 7a, that a much faster drop is reached along τ (values normalized by the norm of singular values vector $\|\Sigma\|$).

At this step, since the development of the modes while traveling can be analyzed better using a DMD, the snapshots which are now in spatiotemporal space will be decomposed using the following algorithm, known as the standard DMD [25]. For this purpose, a linear mapping is then assumed as:

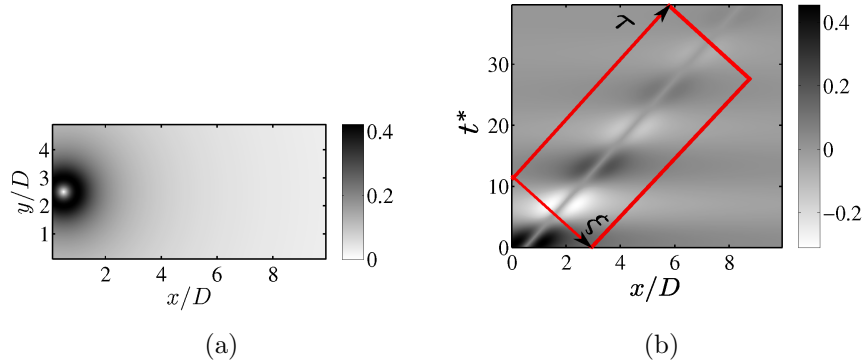


Figure 6: Contours of tangential velocity normalized by $U_{max,i}$ used as the initial condition (a), and space time diagram(b).

$$X' = AX \quad (13)$$

with X and X' being the first and last n snapshots in $X_{0..n}$. The transition matrix A can be approximated using SVD of matrix X ,

$$X = U\Sigma V^T \quad (14)$$

and using the projected matrix \tilde{A} ,

$$\tilde{A} = U^T A U = U^T X' V \Sigma^{-1}. \quad (15)$$

By computing the eigenvalues and eigenvectors of \tilde{A} ,

$$\tilde{A}w = \Lambda w \quad (16)$$

the DMD modes will be given by

$$\phi = U w. \quad (17)$$

What follows in this chapter, clarifies how a DMD in the rotated frame of reference along τ compares with a traditional DMD along t . The red frame in figure 6b ¹ shows the bounds of data which is decomposed in the new frame of reference. For a rotation in $x - t$ plane, the maximum number of

¹Here we note that we do not make use of all data using this approach, specially if the dataset is periodic. This is unlike the method of Rowley and Marsden [22] which implements a pure shift. But as we are not willing to chose the method on economic grounds, there is not much to do about this for the moment.

snapshots that can be acquired in the rotated frame ($n_{\tau(max)}$), is a function of number of snapshots along the time axis (n_t), the group velocity (u_g^*), timestep between the snapshots (dt^*) and the spatial distance between the grid points along x ($dx^* = dx/2R$). Therefore the transformation coefficient of α_t can be defined as:

$$\alpha_t = \sqrt{1 + \left(u_g^* \frac{dt}{dx}\right)^2}, \quad (18)$$

for the ratio of:

$$\frac{n_{\tau(max)}}{n_t} = \alpha_t, \quad (19)$$

stating that for a certain number of snapshots in physical space, the value of $n_{\tau(max)}$ will be essentially larger than n_t . Nevertheless, as it can be inferred from figure 6b, the final value of n_t , is also defined by the choice of frame width along ξ . Furthermore, the latter coefficient also provides a measure for the spatial resolution of the desired structure in the spatiotemporal space $Res_{(st)}$ as:

$$\frac{Res_{(phys)}}{Res_{(st)}} = \alpha_t, \quad (20)$$

with $Res_{(phys)}$ being the spatial resolution in physical space. In other words, if a structures travels in space (x) and time (t) with a constant length and resolution of $Res_{(phys)}$, it will be observed in the rotated frame of reference with resolution of $Res_{(phys)}/\alpha_t$ along ξ . Consequently, to maintain the spatial resolution of the structure in spatiotemporal space, temporal resolution of the snapshots should be adjusted accordingly to keep the value of α_t as close as possible to unity. Therefore, as it holds true for any type of modal decomposition, a high temporal resolution would be crucial for this method as well.

For this test case, transformation coefficient of $\alpha_t = 1.4$ was chosen and the decomposition was carried out acquiring 96 snapshots along τ and 100 snapshots along the time axis on the domain size of $10D \times 5D$ with the resolution of 200×100 in x and y directions respectively.

In the next step the snapshots at all timesteps are projected onto DMD eigenmodes and the modes are sorted by their projection coefficients. Time averaged mode amplitudes are plotted in figure 7b normalized by the norm of full mode for decomposition in both frames. It is clear that the modes decay much faster along the characteristics direction implying that fewer modes will be needed to reconstruct the vortex.

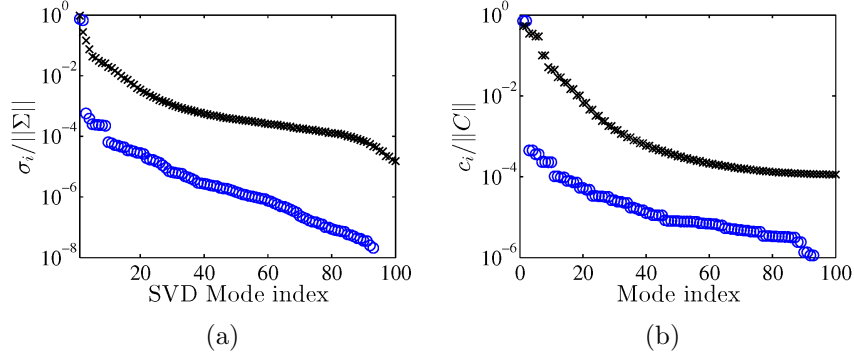


Figure 7: Singular values (a) and modal decay (b) of DMD modes along τ (o) and t (\times).

Having reconstructed the modes in spatiotemporal space, they will be transformed back to physical space. The corresponding eigenvalues calculated in the spatiotemporal space λ_{st} , should be also transformed back to physical space using the rotation angle θ corresponding to the group velocity as:

$$\lambda = \exp\left(\frac{\log \lambda_{st}}{\cos(\theta)}\right). \quad (21)$$

The frequencies and decay rates of (CDMD) modes, will be defined along the physical time, as a function of the timestep between the snapshots dt and rotation angle θ using equations 22 and 23. The eigenvalues in spatiotemporal space are compared against the transformed ones in figures 8a and 8b with the filled markers showing the eigenvalue of the first mode. Dimensionless frequencies and decay rates of CDMD modes are also presented in figure 8c in comparison with those of DMD modes in figure 8d. The blue lines in both figures, show the frequency and decay rate of the vortex, and the filled red markers correspond to the first modes in each reference frame.

$$f^* = \Im\left(\frac{\log \lambda_{st}}{2\pi dt \cos(\theta)}\right), \quad (22)$$

$$d^* = \Re\left(\frac{\log \lambda_{st}}{2\pi dt \cos(\theta)}\right). \quad (23)$$

It can be seen that the first CDMD mode has captured the expected features of the vortex accurately. The DMD modes on the other hand, have

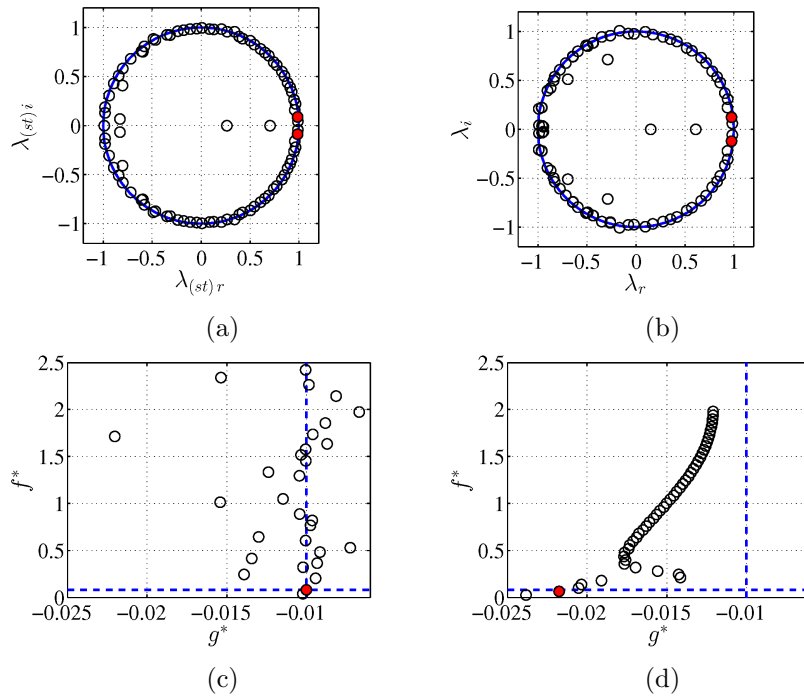


Figure 8: Eigenvalues of \mathcal{CDMD} modes in spatiotemporal space (a) and physical space (b), frequencies and growth rates ($g^* = -d^*$) of the \mathcal{CDMD} modes in physical space (c) and those of \mathcal{DMD} modes (d).

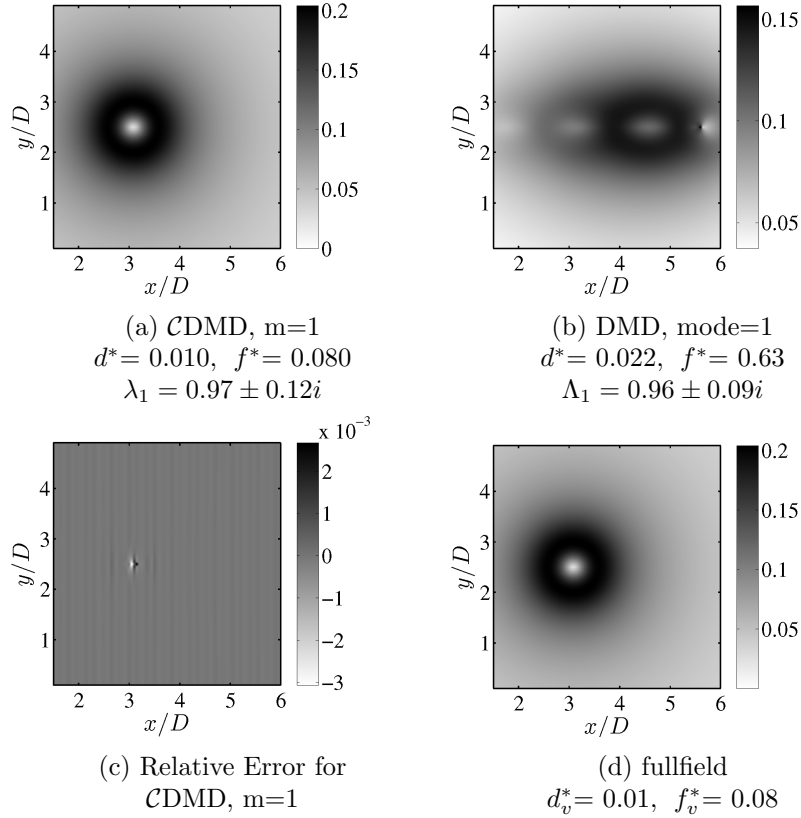


Figure 9: First \mathcal{CDMD} mode reconstructed in physical space (a), fullfield vortex (b), relative error of the first \mathcal{CDMD} mode (c), and reconstruction of the first DMD mode (d) at time $t^* = 12$.

overestimated the decay rate. This is due to the fact that in the original frame of reference the structure moves downstream and therefore this is understood by the DMD as a fast decay rate.

Reconstruction of the first \mathcal{CDMD} and DMD modes at time $t^* = 12$ show the drastic difference between decompositions along the two directions in comparison with the full-field (figures 9a, 9d and 9b). Only one mode along the characteristics suffices to capture the vortex with the mode eigenvalues having correctly detected the expected decay rate and frequency. This is while multitudes of DMD modes are needed along t to reconstruct the vortex. The relative error for the first \mathcal{CDMD} mode is depicted in figure 9c.

Given the example above, the important step in applying the Character-

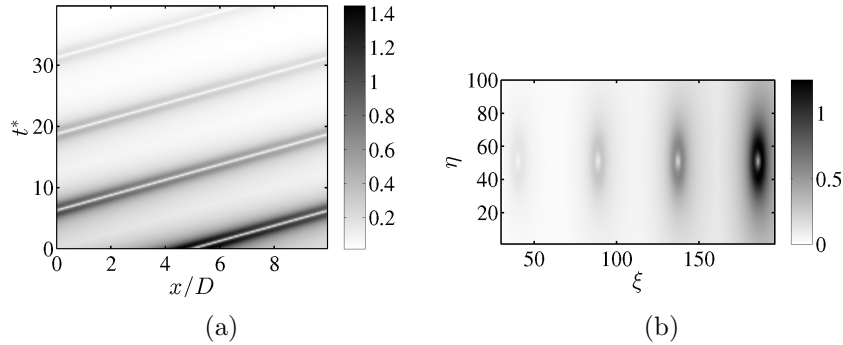


Figure 10: Characteristic diagram for a periodic Lamb-Oseen vortex head (a) and the spatiotemporal representation of the vortex (b).

istic DMD (CDMD) is to take the columns of $X_{0..n}$ normal to the characteristics direction and the rows along it. The resulting structures are defined in planes normal to the group velocity of the structure in space-time. That means they have no immediate temporal or spatial interpretation. For a structure traveling from right to left for instance, the values at the top of the snapshots correspond to a later time than those at the bottom. A backwards rotation in space and time will then result in the spatial representation of the structures.

4.2 Interpretation of periodic data in spatiotemporal space

In order to demonstrate how a set of data with periodicity in the translation direction, can be interpreted in spatiotemporal space, a periodic Lamb-Oseen vortex is considered with the decay rate and frequency of $d^* = 0.01$ and $f^* = 0$ respectively. In this setup, the flow is considered to be periodic in the x direction with the vortex traveling in space with the group velocity of $u_g^* = 0.8$. Space time diagram is depicted in figure 10a where the gradual decay of the periodic vortex can be observed.

By applying a rotation in space and time, with the rotation angle corresponding to the vortex group velocity, one can look at the spatiotemporal representation of the dataset. Along with the transformation, the spatial periodicity is also transformed to accommodate several instances of the same structure in each spatiotemporal set of data at at each point along the characteristics of the flow. Figure 10b, represents one of the spatiotemporal sets along τ .

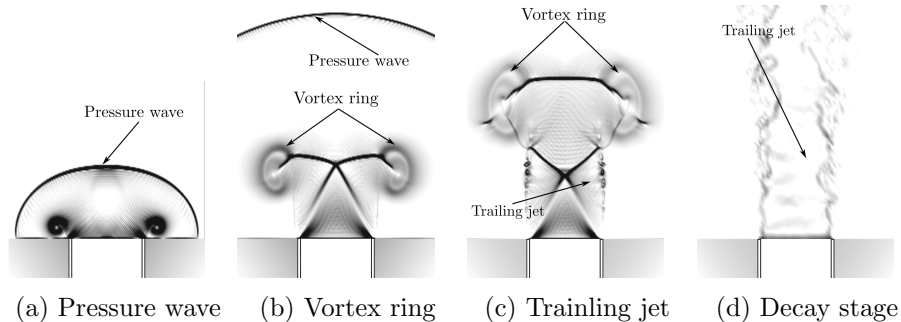


Figure 11: Pseudo-schlieren images of starting jet in time by Pena Fernandez and Sesterhenn [19].

As explained earlier, the structures here do not belong to a certain point in time or space. Rather, they carry spatial information from a range of physical timesteps. As it will be shown in chapter 6, this can be regarded as one of the main reasons why a decomposition along the characteristics will result in a faster drop of singular values, where the events can be described using fewer modes. This example serves only to show how a simple traveling structure can be interpreted in the spatiotemporal space, specially in presence of translational periodicity. In chapter 6, it will be analyzed how this approach compares to looking for the structures in a frame of reference which is shifted only in space with respect to the group velocity.

5 Modal Analysis of a Starting Jet

In this section the method explained above, is applied to existing three dimensional DNS of a starting jet carried out by Pena Fernandez and Sesterhenn [19]. The initial condition in the mentioned study is a tube-like shock, formed by a pressurized reservoir which discharges fluid through a nozzle into an open chamber with ambient pressure. The pressure ratio of $p_1/p_2 = 3.4$ has been chosen to ensure that eventually a supersonic jet will develop. The Reynolds number is approximately $Re = 10^4$ based on the fully expanded conditions. One crucial parameter besides the pressure ratio, is the non-dimensional mass supply of the jet. It can be expressed as the ratio of length to diameter of the pipe L/D . If this ratio is close to unity, a vortex ring will form. In order to develop a trailing jet, the ratio of L/D needs to be larger than 5.

The temporal evolution is shown in figure 11 as a pseudo-schlieren image in a two dimensional cut through the jet and the vortex ring. Figure 11a and 11b show respectively the initial pressure wave and the developing vortex ring at the wall. If enough vorticity is generated, the self-induced velocity of the vortex ring makes it accelerate and travel in flow direction and slightly expand its diameter. Figure 11c shows the vortex ring and the trailing jet, which is formed, if enough mass is supplied. The last image on the right (figure 11d) shows the full jet when the mass supply vanishes and the vortex ring has moved away. We wish to identify the flow for the case of a vortex ring with trailing jet.

5.1 The Vortex Head with Trailing Edge

One of the dominant features of the starting jet is the vortex ring. It is initially formed at the tube lip and detaches later to first move with constant velocity and finally travels with a velocity decaying as square root of time. The aim in this chapter is to detect this vortex and describe it with a few DMD modes. For this test case mass supply ratio of $L/D = 10^7$ has been chosen so that formation of a vortex ring will be followed by trailing edge. For the results presented in this chapter, the decompositions were carried out on 2D cuts of the flow field.

The characteristic diagram is given as space-time plot of the vorticity magnitude along the center of the vortex head in figure 12a, showing the trace of the vortex head traveling in space and time. In this figure $t^* = t/(D/U)$ is the dimensionless time while U and D being the characteristic velocity and the jet diameter respectively. The vortex head is shown in figure 12b at time $t^* = 5.5$.

To detect the optimal direction which also highlights the largest group velocity in the flow, a singular value decomposition is carried out for a range of rotation angles in $x - t$ space and the first 15 singular values are plotted against the rotation angle in figure 13a. The first SVD for $\theta = 0$ is performed on the unrotated snapshots matrix. After that, the snapshots matrix is rotated counterclockwise, with the rotation angle being increased with increments of $\Delta\theta = 0.1$ *radian*.

It is clear in this figure that there is a faster drop for rotation angle $\theta = 1.2$ *radian* which corresponds to the dimensionless velocity of $u^* = u/U = 0.37$, and can be understood as the most dominant group velocity u_g^* in the space-time diagram.

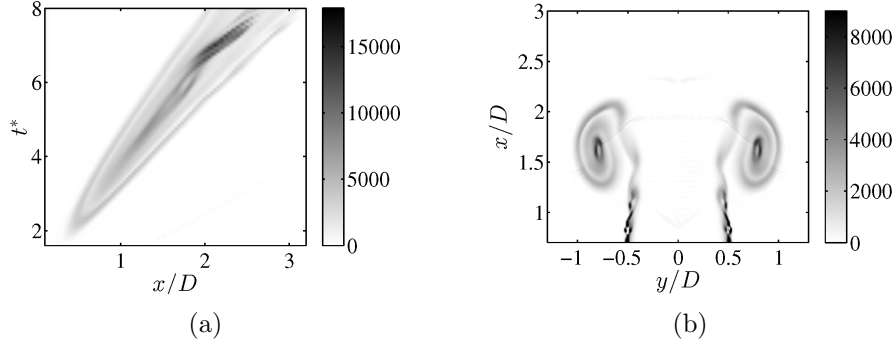


Figure 12: Characteristic diagram along the vortex centerline at $y/D = 0.8$ (a) and the vortex head at time $t^* = 5.5$. Both figures show contour plots of vorticity magnitude.

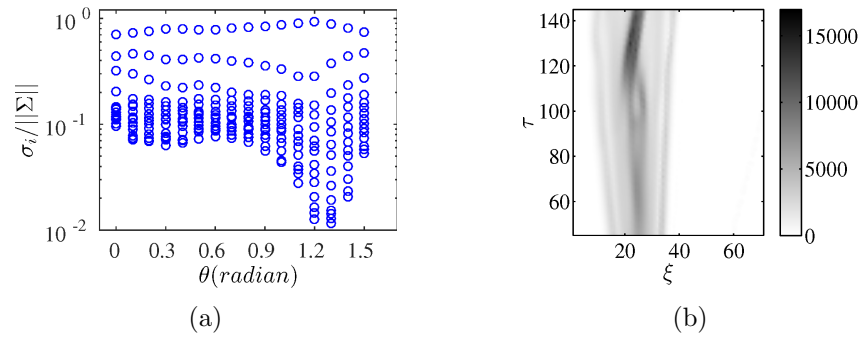


Figure 13: Drop of the first 15 singular values for a range of rotation angles (a) and the characteristic diagram rotated with the optimal angle $\theta = 1.2$ radian, corresponding to the group velocity of $u_g^* = 0.37$ (b).

In the next step, a coordinate transformation of the $xyzt$ -space into the detected direction has to be performed. One can observe in figure 12a that the group velocity changes with time. Thus, to describe the vortex head with the minimum number of modes, also a temporal transformation $t' = \frac{at}{b\sqrt{t+c}}$ with suitable coefficients should be employed. This complication is left for later² and for now the $xyzt$ -cube of data is transformed to the spatiotemporal space treating the data as if the group velocity is constant in time.

The transformation procedure is performed as a decomposition of the rotation matrix into three shears $q' = S_1 S_2 S_1 q$ which is a fast and accurate algorithm [18]. The result is a new $\xi\eta\zeta\tau$ -cube in which a satisfyingly straight part on the characteristic is chosen for modal analysis (figure 13b).

In general, any rotation in four dimensional space can be represented by two rotations in two suitably chosen planes. In our example, where the main flow is in xt -direction, a single rotation in the xt -plane suffices.

Having transformed the data to the spatiotemporal space (with $\alpha_t = 2.64$), a DMD is carried out along τ to capture the spatiotemporal modes. To compare the results with those of a traditional DMD, another decomposition is performed along t on the stationary frame of reference. For this purpose, 65 snapshots were taken along t on a domain size of $4D \times 5D$ with the resolution of 326×600 (in x, y directions) and 100 snapshots were employed along τ with resolution of 70 along ξ .

The yielded modes in both frames are then sorted by their averaged amplitudes. The singular values and Averaged mode amplitudes are compared for both decompositions in figures 14a and 14b, demonstrating a steeper decay and a faster drop in the rotated frame. It is observable that the first 4 CDMD modes represent the snapshots up to a relative remainder of less than 10^{-1} .

²Transformation in time can be achieved by choosing the snapshots equidistantly in t' as defined above. Since abundant time-steps are available from the existing numerical simulation, this can be easily done by choosing the right snapshots. On the other hand, since the vortex head is expanding with time, via a more general approach proposed by Rowley et al [23], also a scaling can be employed. We refer the reader to that article for further information.

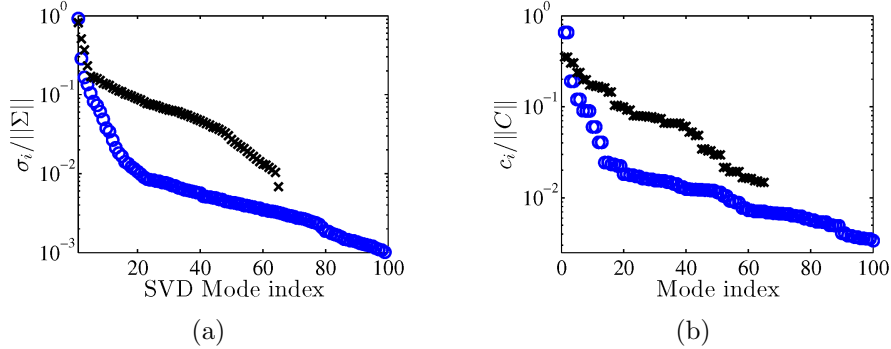


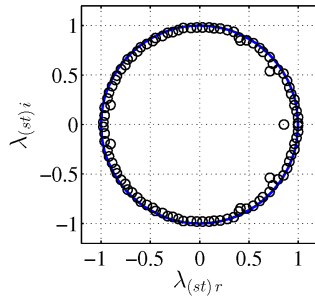
Figure 14: Normalized singular values (a) and modal decay (b) for \mathcal{C} DMD (o) vs. DMD (\times).

The eigenvalues which are resulted from the decomposition along τ are transformed using equation 21 to the physical space. It can be seen in figures 15a and 15c that the eigenvalues resulted in the rotated frame are lying mostly on the unity circle. As expected, by being transformed back, they tend towards inside the circle, signaling a faster decay rate along physical time.

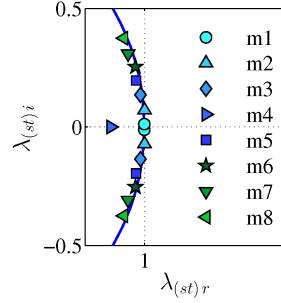
The second effect of this transformation can be noted on the frequency of the modes. The first 8 eigenvalues which are plotted separately in figures 15b and 15d, cover a wider frequency range in the physical space. On the other hand, the DMD on the stationary frame, has captured modes with larger decay rates (figures 15e and 15f). The frequency and decay rate of the modes can be studied more clearly in figure 16.

The first \mathcal{C} DMD mode is captured with a very small decay rate and frequency of $d_c^* = 0.003$ and $f_c^* = 0.06$ implying a rather invariant development in space and time. This mode, having the highest amplitude and lowest decay rate, is shown in figure 17a in spatiotemporal space, and is regarded as one of the suitable candidates for reconstruction of the vortex head. The bounds of the vortex are clearly detected without being smeared or bearing traces of preceding or following timesteps.

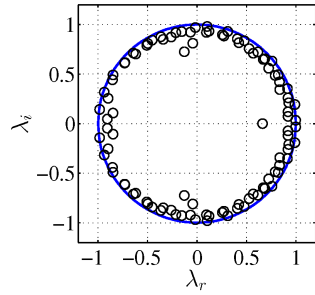
The second mode, contrary to all the other ones, has a small growth rate. This mode is also shown in figure 17b in spatiotemporal space. While the third (figure 17c) and the fifth modes have small decay rates, the fourth mode which is lying far inside the unity circle (figure 15d) with a real eigenvalue, possesses a very large decay rate of $d_c^* = 0.82$ in physical space. Since one of the aims of this chapter is to use a few modes to describe parts of



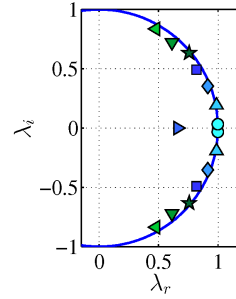
(a) CDMD spectrum in spatiotemporal space



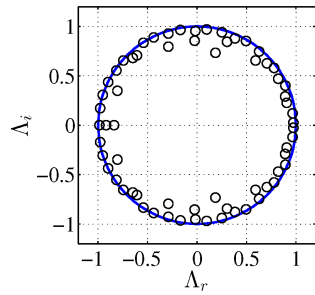
(b) First 8 CDMD eigenvalues in spatiotemporal space



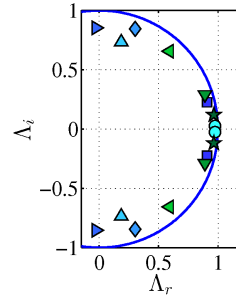
(c) CDMD spectrum in physical space



(d) First 8 CDMD eigenvalues in physical space

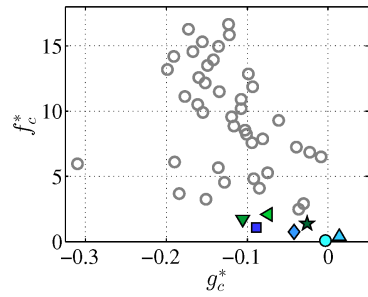


(e) DMD spectrum

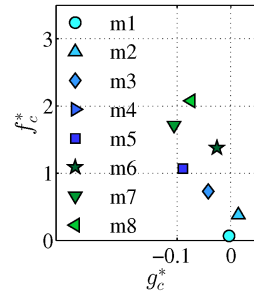


(f) First 8 DMD eigenvalues

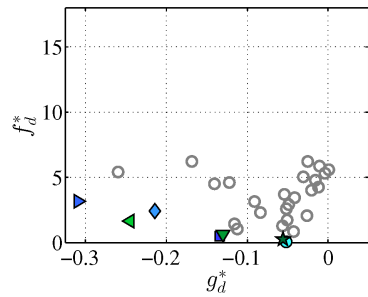
Figure 15: Figures on the left column represent respectively \mathcal{L} DMD spectrum in spatiotemporal space λ_{st} (a), \mathcal{L} DMD spectrum in physical space λ (c) and DMD spectrum Λ (e). The figures on the right column depict the first 8 eigenvalues in the corresponding figure on the left.



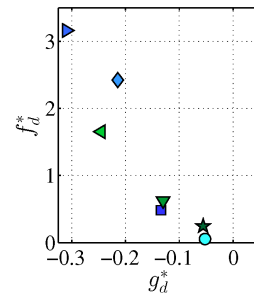
(a) Frequencies and growth rates of CDMD modes in physical space



(b) Frequencies and growth rates of the first 8 CDMD modes in physical space



(c) Frequencies and growth rates of DMD modes



(d) Frequencies and growth rates of the first 8 DMD modes

Figure 16: Dimensionless frequencies and growth rates for CDMD (a,b) and DMD modes (c,d). (indices c and d refer to CDMD and DMD respectively).

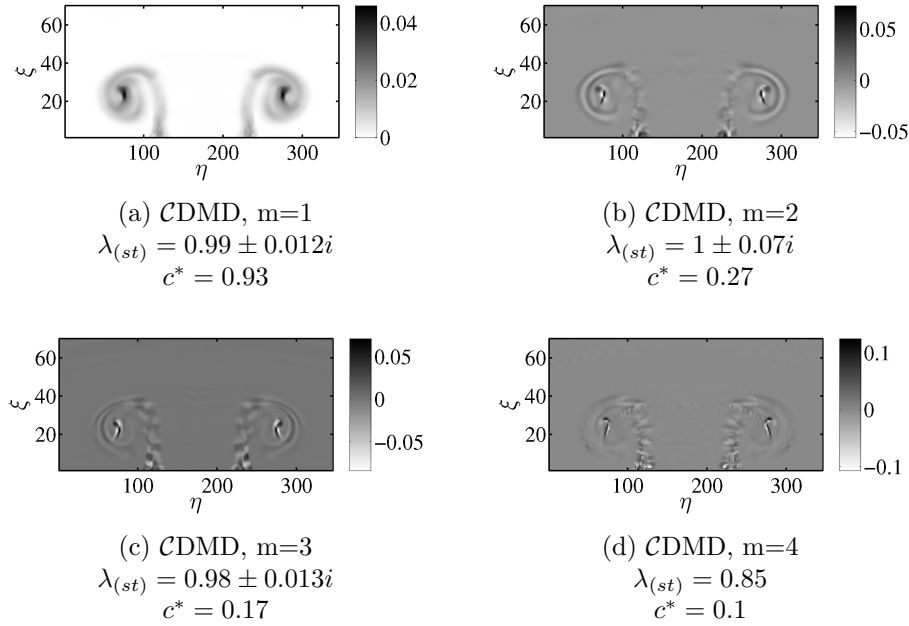


Figure 17: First 4 CDMD modes in spatiotemporal space ($c^* = \langle |c_i| / \|C\| \rangle$) (the real parts of the modes are shown).

the flow that is neither decaying nor growing too fast, therefore this mode (figure 17d) will not be considered as a candidate for reconstruction of the vortex head. It is rather a short lived secondary phenomenon living on that structure.

For the decomposition in the stationary frame, the first mode appears with a strongly smeared picture of the vortex head and with the decay rate of $d_d^* = 0.52$ which is rather large for the first mode compared with that of the first CDMD mode. This mode has captured dominant traces of the shear layer as it will be also demonstrated later for the its reconstruction. The second, third and fourth modes, have relatively higher decay rates of $d_d^* = 0.5, 0.2$ and 0.3 respectively. Therefore, given the discussion above, these modes are not selected for the vortex head reconstruction either. The first two DMD modes are shown in figure 18.

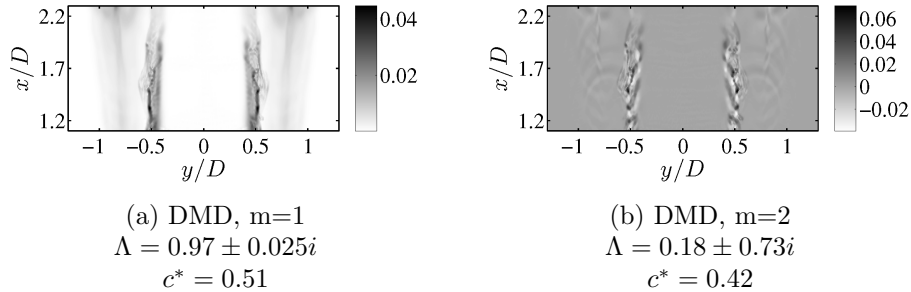


Figure 18: First 2 DMD modes ($c^* = \langle |c_i| / \|C\| \rangle_t$) (The real parts of the modes are shown).

In the next step, the four \mathcal{C} DMD modes that are selected to represent the vortex head, have been reconstructed along τ and then transformed back to physical space as illustrated in figure 19 at time $t^* = 5.6$. The DMD modes on the other hand, are reconstructed along t and confronted against the \mathcal{C} DMD modes in the same figure for the same timestep.

As the vortex ring propagates downstream at the dominant group velocity, the traditional DMD detects instances of the same structure at different spatial locations. As a result, spurious shadows are introduced in each mode behind and ahead of the vortex ring (figures 19b, 19d, 19f& 19h). Therefore, many modes would be required in order to cancel out the shadows and to reconstruct the expected form of the structure.

On the contrary, the Characteristic DMD follows the vortex ring in space-time adjusted to its group velocity and results in a clear representation of the vortex head with the first mode (figure 19a). Each of the next modes in figures 19c, 19e & 19g subsequently accommodate parts of the vortex head, propagating at different frequencies and decay rates, without being smeared or adversely affected by the vortex being transported.

Summation of the four elected \mathcal{C} DMD modes are shown in figure 20a at time $t^* = 5.6$ and confronted against the summed up DMD modes in figure 20b. The vortex head reconstructed by \mathcal{C} DMD is almost indistinguishable from the fullfield depicted in figure 20d. The vortex head itself, was extracted nicely in a single mode as shown before. But the structures with finer scales inside the vortex head move with a slower group velocity as they travel backwards with respect to the main head motion. Therefore, more than one mode was required to capture them. That means, the internal structures of the jet head suffers again from the same deficiencies as did the whole structure before.

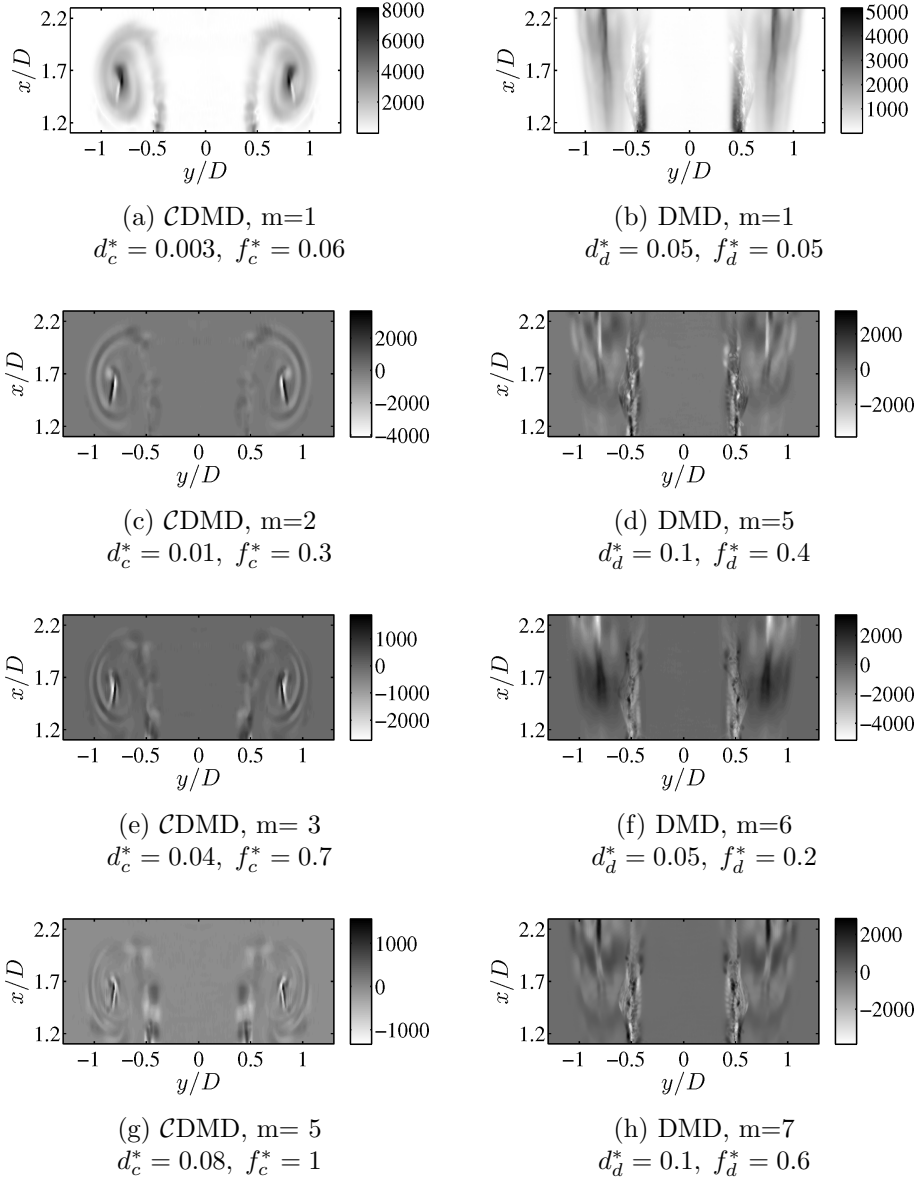


Figure 19: Reconstruction of 4 single \mathcal{CDMD} (left column) and \mathcal{DMD} (right column) modes at time $t^* = 5.6$.

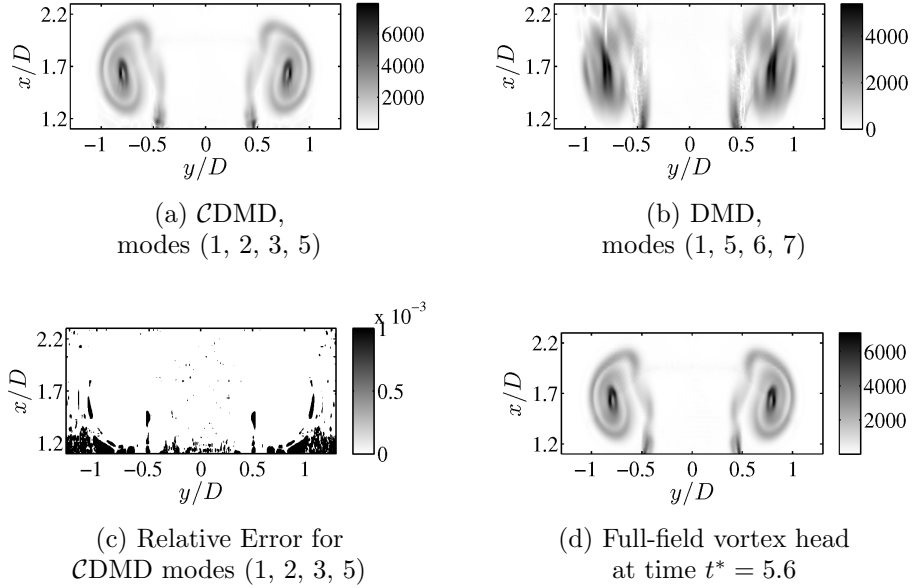


Figure 20: Reconstruction of 4 CDMD (a) and DMD (b) summed up modes at time $t^* = 5.6$, relative error for the CDMD modes (c) in comparison with the fullfield (d).

Nevertheless, already four CDMD modes give a clear resemblance of the full structure while the same number of DMD modes fail to represent even the boundaries of the vortex head. The same holds true for the structures of the shear layer on the trailing jet, as it moves with a faster velocity than the vortex head and to capture these structures the same practice should be applied using the velocity of the trailing edge.

To quantify the accuracy by which the structures have been captured, the relative error is calculated for the resulted reconstruction in figure 20c. The area on the vortex head shows clearly less than 0.1% relative error. By looking into the reconstructed part of characteristic diagram, it is observable that the same agreement between the fullfield and CDMD modes, holds also valid for the rest of the timesteps (figure 21). The space time diagram reconstructed using CDMD modes, has captured many of the details originally existing in the fullfield. As expected of course, the DMD reconstruction has led to a vague reproduction of the field, missing out many of the details which can be only captured using many modes.

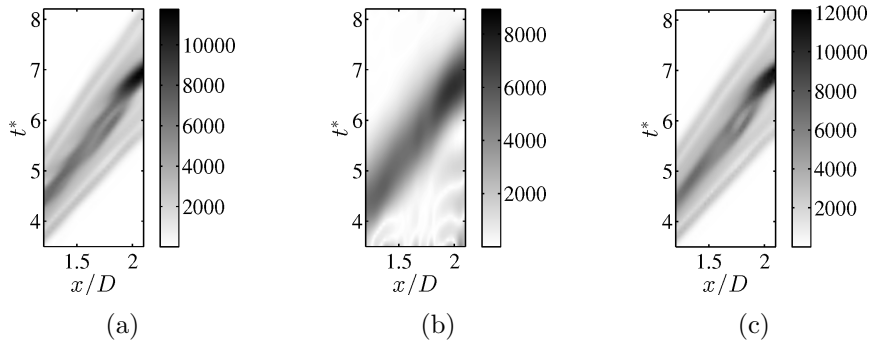


Figure 21: Characteristic diagram reconstructed using 3 \mathcal{CDMD} (a) and DMD (b) modes in comparison with the fullfield (c).

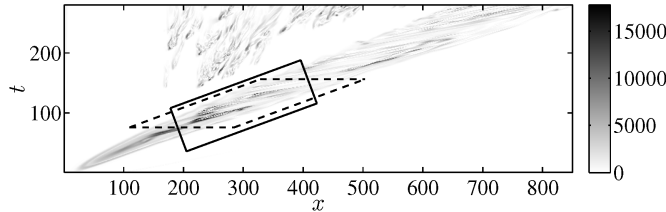


Figure 22: Characteristic diagram at the center of the vortex head at $y/D = 0.8$. Solid and dashed windows correspond respectively to a decomposition window in the spatiotemporal and shifted space.

6 Spatiotemporal vs. spatial decomposition

What sets our proposed method apart from similar studies in the past, is that via a Characteristic DMD, moving structures are detected in spatiotemporal space in planes normal to the characteristics, while in other data-driven methods, they are sought in a shifted space. In order to clarify the differences between the two approaches, a comparative analysis is presented in this chapter between the Characteristic DMD (\mathcal{CDMD}), Shifted DMD (\mathcal{SDMD}) and a traditional DMD. For this purpose, and to verify the dependence of the decompositions on the number of snapshots, the turbulent stage of the vortex head has been selected. This is due to the fact, that as shown in figure 22, the time span during which the vortex head remains turbulent, is longer than the laminar development of the vortex head.

As illustrated in figure 23 two different transformations have been applied to the snapshots matrix, both corresponding to the same group velocity

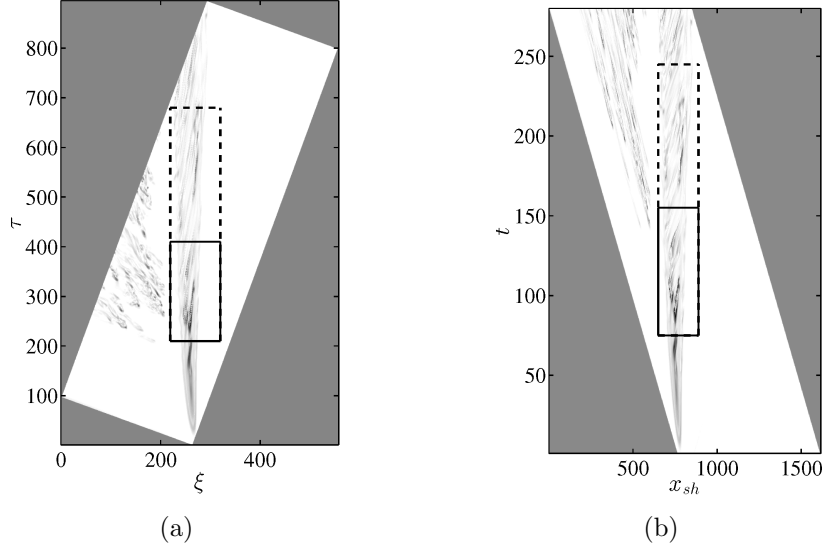


Figure 23: Transformed snapshots matrix in the spatiotemporal (a) and shifted (b) reference frames.

$u_g^* = 0.4$. Applying a rotation in space and time, the snapshots matrix with columns and rows along x and t , has been transformed to a spatiotemporal space, resulting in a matrix with columns and rows along ξ and τ (figure 23a). Via another transformation in form of a shift in space, the snapshots matrix has been transformed to a shifted space, aligning the columns and rows of the resulted matrix along x_{sh} and t (23b). The space time diagrams in this figure, are both taken along the stream wise direction at the center of the vortex head. Figures 22 and 23 are both plotted in computational space with the axes corresponding to the relevant matrix elements.

To examine the the dependence of the dynamics of the resulted modes on the number of snapshots, ten decomposition windows have been selected for each set of transformed data. Each of the ten windows in the rotated frame are comparable with the corresponding one in the shifted one. On each frame of reference, all ten windows have the same spatial extents accommodating the vortex heads and excluding the trailing jet. This choice has been made due to the fact that the two mentioned parts, have different group velocities and with this analysis we are aiming at treating only the vortex head. Extra space has been allowed downstream of the vortex head to have a measure of how well each decomposition has captured the bounds of the vortex ring.

The temporal extents have been chosen to ensure maximum overlap be-

tween each two corresponding windows in the rotated and shifted frames. To demonstrate the latter, the smallest window in each frame, is plotted in physical space in figure 22 as solid and dashed lines representing the rotated and shifted decomposition windows respectively. As it can be seen in this figure, the lower and upper bounds of the two illustrated windows, coincide exactly at the center of the vortex ring. The same holds true for all the decompositions.

While keeping the lower temporal extent fixed, the upper temporal bounds have been incrementally increased for each window. The increments along τ in spatiotemporal space i_τ and along t in the shifted space i_t are related as $i_\tau = \alpha i_t$, with α defined by equation 19. Solid and dashed black lines in figure 23 correspond respectively to the bounds of the smallest and largest windows.

The gray areas in both figures, show the zeros which have been added to the snapshots matrix via the transformations. The first observation at this point, is that the full dataset can be used neither in the rotated nor in the shifted space. In other words, while treating non-periodic data, both methods will essentially lead to a certain level of data loss. This limitation will not exist in the shifted decomposition for periodic datasets.

In the next step, a singular value decomposition is carried out on each frame of reference and for each window. In figure 24, singular values resulted in the rotated and shifted frames are plotted in blue and green respectively with the darker colors depicting the larger decomposition windows. As expected, as the number of snapshots increases, a slower drop of singular values is resulted in both frames. But It can be observed that for all decompositions, there is a faster drop of singular values in the spatiotemporal space. This means that independent of the number of snapshots, the vortex ring can be reduced using fewer modes in the spatiotemporal space in comparison with the shifted space.

Next, a standard DMD is carried out for each of the windows and the resulted modes are sorted based on their average contribution in all the timesteps. The cumulative mode amplitudes are plotted for *CDMD* and *SHDMD* in figure 25. It can be observed that the first 2 or 3 modes in the spatiotemporal space, have a higher cumulative content than the same number of modes in the shifted space.

To reach an elaborate assessment of the modes and their evolutions in space and time, one of the ten groups of decompositions have been selected

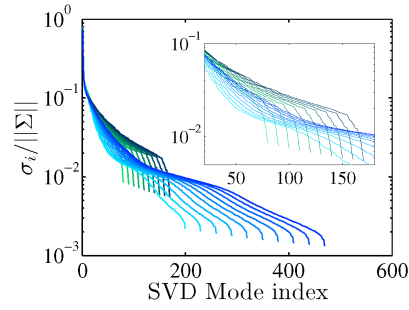


Figure 24: Singular values in spatiotemporal and shifted reference frames presented respectively in blue and green. Darker colors correspond to larger windows.

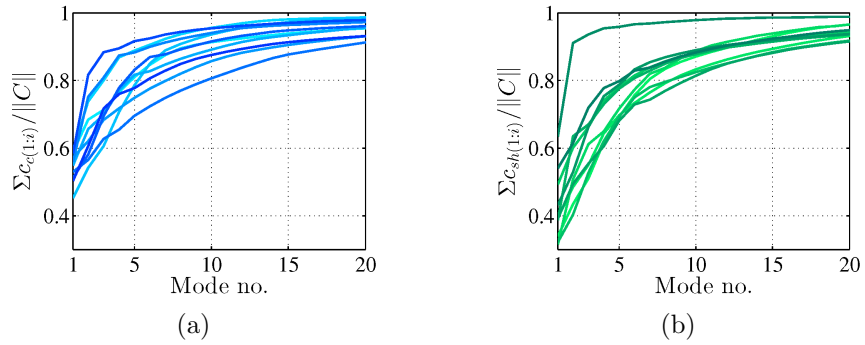


Figure 25: Cumulative mode contents in the spatiotemporal (a) and shifted (b) reference frames.

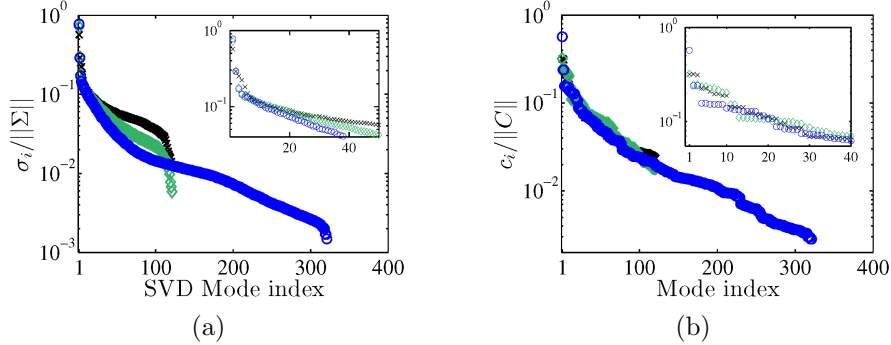


Figure 26: Singular values (a) and mode contents (b) in the spatiotemporal (○), shifted (◇) and stationary (×) reference frames.

with 320 and 120 number of snapshots along τ and t respectively. To compare the results with a traditional DMD in physical space, another decomposition is also carried out on a stationary frame of reference. The temporal bounds for the latter DMD, are similar to those selected for the \mathcal{SHDMD} .

The resulted singular values are shown in figure 26a with blue circles, green squares and black crosses representing the rotated, shifted and physical spaces respectively. Since via the spatiotemporal and the shifted transformations, the vortex head is being followed on a moving frame of reference, an SVD leads to a faster drop of singular values compared to the singular values in physical space. Nevertheless, as mentioned earlier, the fastest drop happens along τ .

For the three mentioned dynamic mode decompositions in spatiotemporal, shifted and physical spaces, mode amplitudes are plotted in figure 26b with the symbol colors similar to what was defined earlier. It can be seen in this figure and in its magnified part, that except for the first 10 modes, the overall trend of the modal content is not hugely different for the three decompositions. This similarity can be explained by the fact that the vortex ring and the events inside it are traveling at different velocities as it can be seen in figure 22. To capture these events efficiently, a transformation to a different frame of reference would be required.

The result is that on a frame of reference which is chosen by the group velocity of the vortex head, many modes will be still needed to capture the events inside, which are traveling at a different velocity. Therefore except for the first few modes, the modal decay will follow the same trend as that

of the DMD modes on physical space. In other words, all three decompositions treat the mentioned instabilities similarly and the main difference is noticeable only for the part of the flow, whose group velocity is closest to the velocity of the moving frame.

Similar to the analysis in the previous section, it is the vortex head which fits most closely the definition of a coherent structure, and therefore the frame of reference is chosen based on this coherent part of the flow. The first 10 mode amplitudes show that the decomposition on each frame of reference, treats the vortex head differently. While a \mathcal{CDMD} along the characteristics leads to the first mode with average amplitude of $c_c = 0.57$, the first \mathcal{SHDMD} and DMD modes have amplitudes of $c_{sh} = 0.33$ and $c_d = 0.31$ respectively. To reach a cumulative mode content of 0.57, 3 modes have to be taken on each of the other frames. Taking 12 modes will amount to cumulative mode contents of $c_c^* = 0.88$ along τ , $c_{sh}^* = 0.85$ along t in the shifted space and $c_d^* = 0.87$ along t in the physical space.

The first modes and summations of the first 12 modes are reconstructed in the rotated and shifted frames and transformed back to physical space, in order to compare the reduced vortex head in the physical space (figure 27) between the three methods. The mentioned reconstructed modes are plotted in figure 28 at the same physical time $t^* = 13.7$. To present an overview of all the timesteps, space-time diagram reconstructed using 12 modes in each frame, is depicted in figure 29 and compared against the fullfield. For each decomposition, the spectrum is presented in form of dimensionless decay rates and frequencies for the first 30 modes in figure 30 along with the time averaged mode contents in each frame. In this figure, complex conjugate mode amplitudes and eigenvalues are presented only once for each mode. The spectrum presented for the decomposition in spatiotemporal space, is resulted by transformation from spatiotemporal to physical space by equations 22 and 23.

As expected, DMD modes captured on the stationary frame of reference, fail to describe a clear picture of the vortex head (figures 28e and 28f). The first mode represents a smeared trace of the vortex ring distorted by the trailing jet which requires many modes to be added to reach a more clear reconstruction of the large-scale features of the flow. But even after adding 12 modes, the result is still far beyond sufficient. The same can be observed in all other timesteps as demonstrated in the reconstructed space-time diagram in figure 29d using 12 DMD modes. Unlike the first modes on the moving reference frames, which both possess a zero frequency, the eigenvalue of the first DMD mode shows frequency of $f_d^* = 0.2$. The first

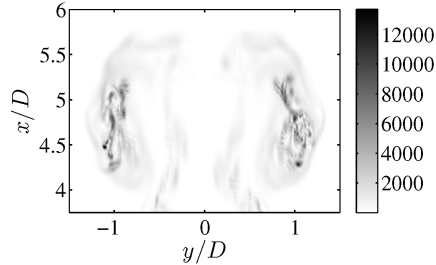


Figure 27: Representation of the fullfield vortex head at time $t^* = 13.7$.

DMD mode also has a larger decay rate of $d_d^* = 0.07$ compared to the first modes in the rotated and shifted spaces.

Both decompositions on the shifted and rotated frames, deliver much better descriptions of the vortex head with the first mode, while the borders of the vortex head appear to be more distinct in the first \mathcal{CDMD} mode. The first \mathcal{CDMD} and \mathcal{SHDMD} modes have respectively decay rates of $d_c^* = 0.02$ and $d_{sh}^* = 0.006$. Adding up 12 modes for each decomposition, will capture most of the large scale features of the vortex head. The reconstructed space-time diagram using 12 modes for each analysis in figure 29, provides a good measure of how well all timesteps have been described using 12 modes. While both methods have captured the overall shape of the vortex ring in all timesteps, closer resemblance is observable between the fullfield and the \mathcal{CDMD} reconstruction.

The observed differences between the \mathcal{CDMD} and \mathcal{SHDMD} results, can be explained by the fact that, the modes and the structures in spatiotemporal space, do not contain only spatial information about the flow, as they do not belong to only one timestep. Rather, each spatiotemporal mode or structure, carries information about its history, its present state and its future.

7 Summary and Conclusion

In this study a modal decomposition was carried out along the characteristics direction given by the group velocity of a structure allowing the extraction of the moving features. Using this approach, we seek to define the structures in planes normal to the direction of the characteristics. This means they are defined as coherent events in space and time, as opposed to a snapshot

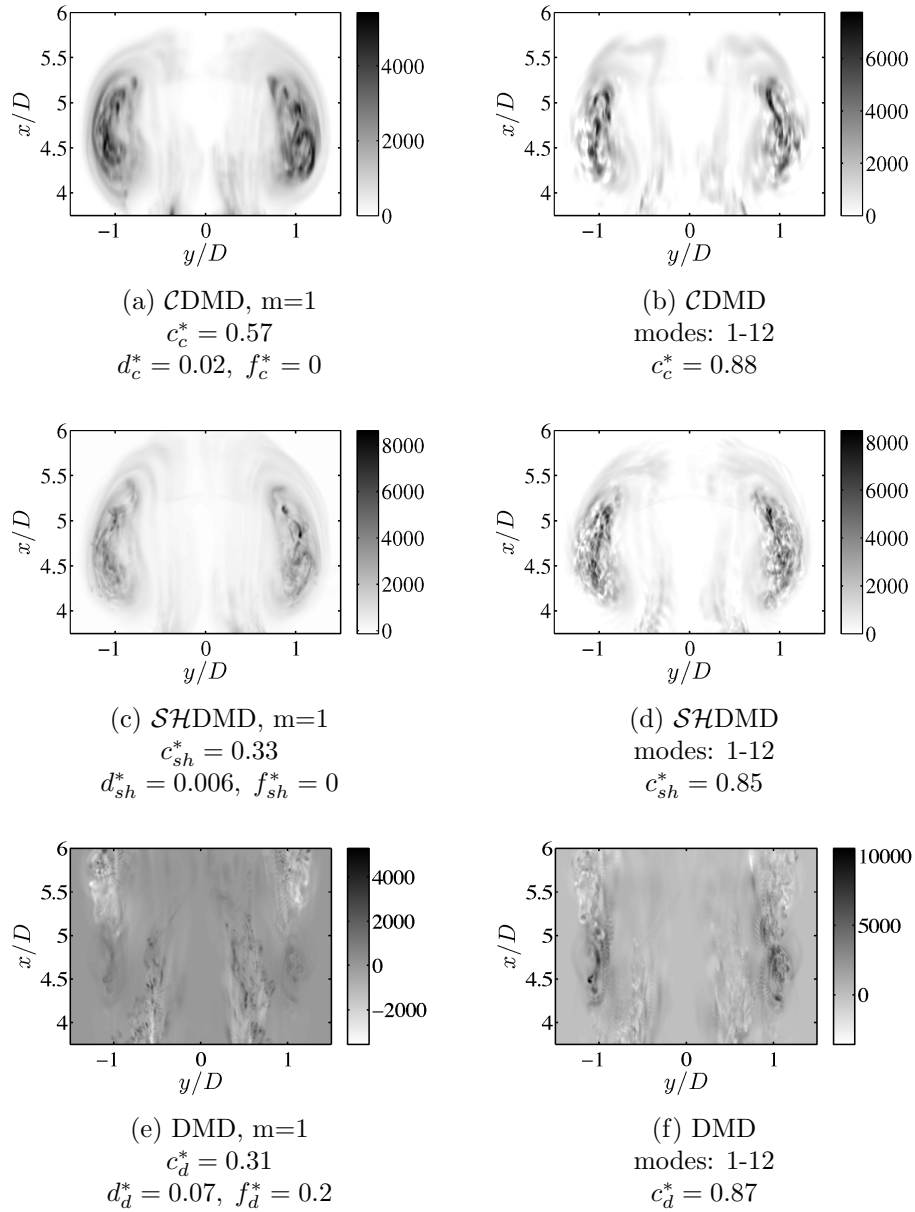


Figure 28: Reconstruction of the first mode (left column) and the first 12 modes (right column) for \mathcal{CDMD} (a,b), \mathcal{SHDMD} (c,d) and \mathcal{DMD} (e,f) at timestep $t^* = 13.7$.

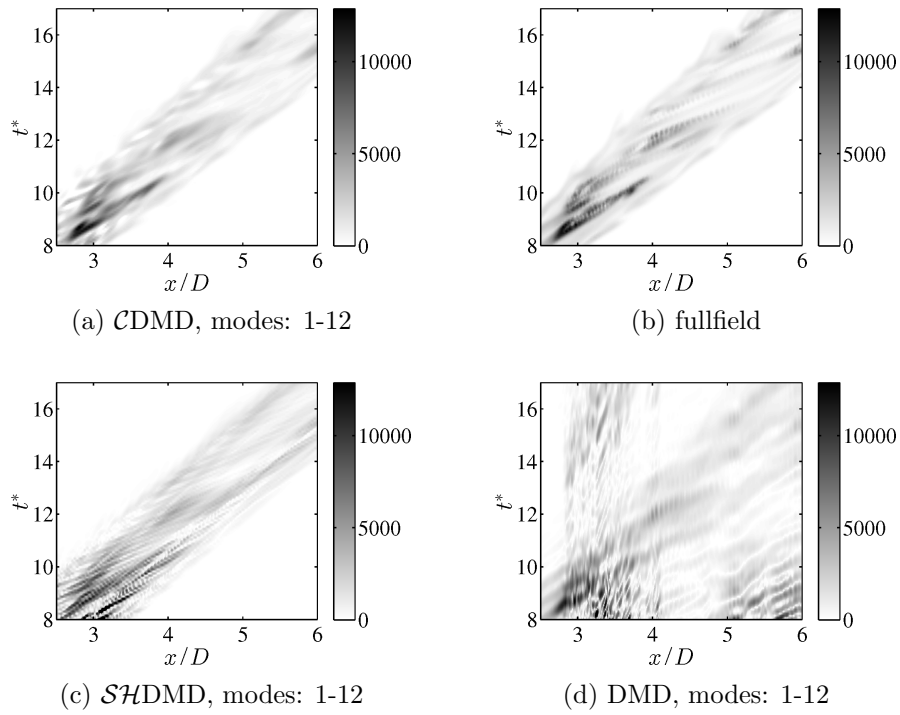
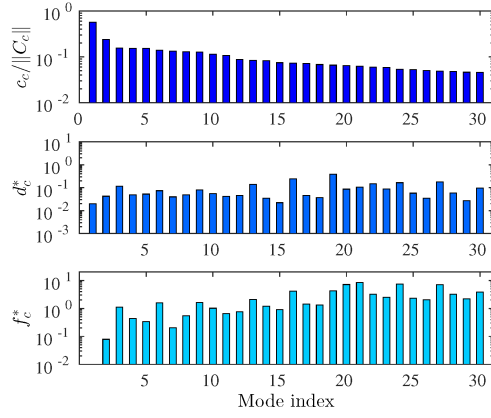
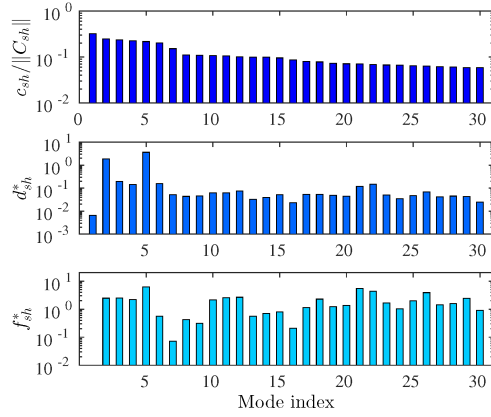


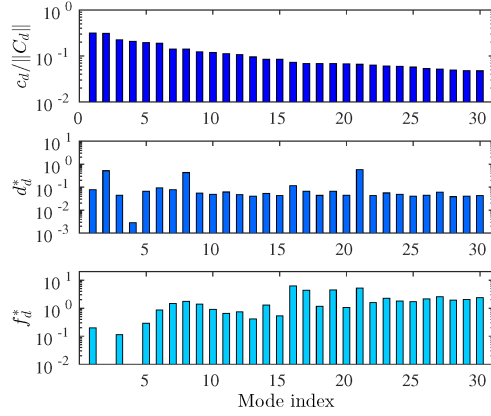
Figure 29: Space time diagram plotted at the center of the vortex head, reconstructed using 12 $CDMD$, $SHDMD$ and DMD modes, compared against the fullfield.



(a)



(b)



(c)

Figure 30: Mode amplitudes, dimensionless decay rates and frequencies for the first 30 \mathcal{C} DMD (a), $\mathcal{S}\mathcal{H}$ DMD (b) and DMD (c) modes.

in time or a time series at a fixed location. To fulfill this purpose, one rotation in four dimensional space would be necessary. In general, this can be done by two rotations, but in the studied case of a jet, the main direction coincides with one of the axis and therefore one rotation was sufficient. In the rotated frame, a modal decomposition was performed and the vortex head of a starting jet was extracted with a few modes only.

The physical structure was recovered after rotation back into the physical frame, where the results were compared against a traditional DMD carried out on a stationary frame of reference. This comparison revealed a much faster drop of singular values along the characteristics. The vortex head, that was treated as a coherent structure with a small decay rate, was reconstructed much more accurately using a *CDMD*. The borders were distinctly captured with only one mode, and adding 4 spatiotemporal modes provided a very good description of the instabilities inside the vortex head.

In the final chapter, a comparison was carried out between a characteristic DMD and a shifted DMD, extracting the modes in a rotated and a shifted frame respectively. The dependence of the decompositions on the number of snapshots was also verified by employing 10 different windows in each frame of reference. It was shown that a singular value decomposition, led to a faster drop of singular values in all the windows along the characteristics in the rotated reference frame. Both methods resulted in considerable improvements in describing the vortex head in comparison with a traditional DMD. Nevertheless, reconstructing the first mode and the summed up first 12 modes for each method, the *CDMD* modes appeared to capture the large-scale feature of the flow more efficiently with fewer modes.

Using the introduced approach, transport-dominated structures as well as their development along their paths can be described. The method can be used for the definition of empirical coherent structures with discreet translational symmetry, given as a reduced order model described by a few modes.

Acknowledgements: The authors would like to gratefully acknowledge Juan José Peña Fernández for providing simulated data for this study. Major parts of this work were performed during the sabbatical leave of the first author in 2015. He wishes to thank, both his own university as well as La Sapienza, Rome, for this opportunity. The second author would like to appreciate Prof. Christoph Egbers (Brandenburg University of Technology - BTU Cottbus - Senftenberg), for the invaluable support during this research.

References

- [1] Adrian RJ (2007) Hairpin vortex organization in wall turbulence. *Phys Fluids* 19:041301
- [2] Adrian RJ, Meinhardt CD, Tomkins CD (2000) Vortex organization in the outer region of the turbulent boundary layer. *J Fluid Mech* 422:1–54
- [3] Avila M, Mellibovsky F, Roland N, Hof B (2013) Streamwise-localized solutions at the onset of turbulence in pipe flow. *Phys Rev Lett* 110:224,502
- [4] Bakewell HP, Lumley JL (1967) Viscous sublayer and adjacent wall region in turbulent pipe flow. *Physics of Fluids* 10(9):1880–1889
- [5] Balakumar BJ, Adrian RJ (2007) Large- and very-large-scale motions in channel and boundary-layer flows. *Philos Trans R Soc Lond A* 365:665–81
- [6] Chong MS, Perry AE, Cantwell BJ (1990) A general classification of three dimensional flow fields. *Physics of Fluids A* 2(5):765–777
- [7] Faisst H, Eckhardt B (2003) Traveling waves in pipe flow. *Phys Rev Lett* 91:224,502
- [8] Glauser MN, Leib SJ, George WK (1987) *Coherent Structures in the Axisymmetric Turbulent Jet Mixing Layer*, Springer Berlin Heidelberg, Berlin, Heidelberg, pp 134–145
- [9] Haller G (2005) An objective definition of a vortex. *J Fluid Mech* 525:1–26
- [10] Hellström LHO, Smits AJ (2014) The energetic motions in turbulent pipe flow. *Physics of Fluids* 26(12):125102
- [11] Hellström LHO, Sinha A, Smits AJ (2011) Visualizing the very-large-scale motions in turbulent pipe flow. *Physics of Fluids* 23(1):011703
- [12] Hunt JCR, Wray AA, Moin P (1988) Eddies, stream, and convergence zones in turbulent flows. Center For Turbulence Research Report CTR-S88
- [13] Hutchins N, Marusic I (2007) Large-scale influences in near-wall turbulence. *Philos Trans R Soc Lond* 365:647–64

- [14] Jeong J, Hussain F (1995) On the identification of a vortex. *J Fluid Mech* 285:69–94
- [15] Lumley JL (1967) The structure of inhomogeneous turbulent flows. *Atmospheric turbulence and radio wave propagation* pp 166–178
- [16] Lumley JL (1981) Coherent structures in turbulence. In: Meyer RE (ed) *Transition and Turbulence*, pp 215–242
- [17] Mezic I (2013) Analysis of fluid flows via spectral properties of the koopman operator. *Annu Rev Fluid Mech* 45:357–78
- [18] Paeth AW (1990) *Graphics gems*. Academic Press Professional, Inc., San Diego, CA, USA, chap A Fast Algorithm for General Raster Rotation, pp 179–195
- [19] Pena Fernandez J, Sesterhenn J (2017) Compressible starting jet: Pinch-off and vortex ring-trailing jet interaction. *Journal of Fluid Mechanics* 817:560–589, DOI 10.1017/jfm.2017.128
- [20] Reiss J, Schulze P, Sesterhenn J (2015) The shifted proper orthogonal decomposition. arXiv:151201985v1 [mathNA]
- [21] Rosenberg BJ, Hultmark M, Vallikivi SCCB, Smits AJ (2013) Turbulence spectra in smooth- and rough-wall pipe flow at extreme reynolds numbers. *J Fluid Mech* 731:46–63
- [22] Rowley CW, Marsden JE (2000) Reconstruction equations and the karhunen–loève expansion for systems with symmetry. *Physica D: Nonlinear Phenomena* 142(1–2):1 – 19
- [23] Rowley CW, Kevrekidis IG, Marsden JE, Lust K (2003) Reduction and reconstruction for self-similar dynamical systems. *Nonlinearity* 16(4):1257
- [24] Rowley CW, Mezić I, Bagheri S, Schlatter P, Henningson DS (2009) Spectral analysis of nonlinear flows. *Journal of Fluid Mechanics* 641:115–127
- [25] Schmid PJ (2010) Dynamic mode decomposition of numerical and experimental data. *J Fluid Mech* 656:5–28
- [26] Schmid PJ, Sesterhenn J (2008) Dynamic mode decomposition of numerical and experimental data. *Amer Phys Soc, 61st APS meeting* p 208

- [27] Sharma AS, Mezić I, McKeon BJ (2016) Correspondence between koopman mode decomposition, resolvent mode decomposition, and invariant solutions of the Navier-Stokes equations. *Phys Rev Fluids* 1:032,402
- [28] Sirovich L (1987) Turbulence and the dynamics of coherent structures. i - coherent structures. ii - symmetries and transformations. iii - dynamics and scaling. *Quarterly of Applied Mathematics* 45:561–571
- [29] Vallikivi M, Ganapathisubramani B, Smits AJ (2015) Spectral scaling in boundary layers and pipes at very high reynolds numbers. *J Fluid Mech* 771:303–326
- [30] Waleffe F (1998) Three-dimensional coherent states in plane shear flows. *Phys Rev Lett* 81:4140–4143
- [31] Wu X, Moin P (2009) Direct numerical simulation of turbulence in a nominally-zero-pressure-gradient flatplate boundary layer. *J Fluid Mech* 630:5–41